POLITECNICO DI TORINO
Repository ISTITUZIONALE

Geometrical scale down analyses of the EU-DEMO WCLL BZ water U-manifolds

Original
Geometrical scale down analyses of the EU-DEMO WCLL BZ water U-manifolds / Corrado, M., Arena, P., Collaku, A., Del Nevo, A., Marinari, R., Savoldi, L.. - In: FUSION ENGINEERING AND DESIGN. - ISSN 0920-3796. - ELETTRONICO. - 230:(2026). [10.1016/j.fusengdes.2026.115890]

Availability:
This version is available at: 11583/3015117 since: 2026-09-02T16:17:31Z

Publisher:
Elsevier Ltd

Published
DOI:10.1016/j.fusengdes.2026.115890

Terms of use:

This article is made available under terms and conditions as specified in the corresponding bibliographic description in the repository

Publisher copyright

(Article begins on next page)

21 November 2026

Fusion Engineering and Design 230 (2026) 115890

Contents lists available at ScienceDirect

Fusion Engineering and Design

journal homepage: www.elsevier.com/locate/fusengdes

Review

Geometrical scale down analyses of the EU-DEMO WCLL BZ water U-manifolds

Marino Corrado [a,*], Pietro Arena [b], Aldo Collaku [a], Alessandro Del Nevo [b], Ranieri Marinari [b], Laura Savoldi [a]

[a] MAHTEP Group, Dipartimento Energia "Galileo Ferraris", Politecnico di Torino, Italy
[b] ENEA Brasimone Research Center, Bacino del Brasimone 1, Camugnano, (Bologna), 40032, Italy

ARTICLE INFO

Keywords:
EU DEMO
Water-cooled lithium lead breeding blanket
U-type coolant manifold
Thermal-hydraulic scaling
CFD flow distribution

ABSTRACT

A geometrically scaled-down Test Section representative of the Outboard Segment water manifold of the European DEMO Water-Cooled Lithium Lead Breeding Blanket has been designed for experimental investigation in the Water Loop facility of the W-HYDRA platform, currently under construction at the ENEA Brasimone Research Center. The Test Section is designed to experimentally validate the coolant mass flow rate distribution among parallel Breeding Units (BUs) in the full-scale manifold and to provide experimental confirmation of the numerical tools and modelling assumptions adopted in the blanket design. Building on previous studies addressing the scaling and modelling of a Z-type manifold configuration, the present work focuses on a U-type manifold layout, which ensures a more uniform flow distribution among BUs. A scaling factor of four is applied to the manifold length, cross-sectional areas, number of breeding units and total inlet mass flow rate, while preserving the coolant velocity profiles along the manifolds. This approach allows each BU of the Test Section to be hydraulically representative of four BUs of the full-scale design. The coolant channels within the breeding units are modelled through equivalent porous pipes, enabling a substantial reduction of the computational cost while preserving the hydraulic characteristic. Steady-state single-phase Computational Fluid Dynamics simulations of the Test Section are performed using the same modelling framework adopted for the full-scale configuration, including identical operating conditions, turbulence modelling and numerical settings. The results demonstrate that the mass flow rate distribution within the BUs is preserved with a relative error $< 10\%$, while the distribution among the BUs is preserved within 3% for all units except the inlet one, which is affected by jet entrance effects. The analysis confirms that pressure losses within the BUs dominate the overall pressure drop and can be effectively preserved through a pressure-profile-based scaling. Minor limitations introduced by the scale-down, such as enhanced inlet jet effects and vortex instabilities near the manifold extremities, are identified and discussed, providing guidance for future design optimizations of the experimental Test Section.

1. Introduction

The European demonstration fusion power plant (EU-DEMO) represents a critical milestone in the European fusion roadmap [1], consisting of a tokamak reactor producing 300–500 MW of net electrical power while operating with a closed Deuterium–Tritium fuel cycle. Unlike its predecessor ITER, which prioritizes physics exploration and optimization, DEMO is engineered to achieve continuous net electricity production and demonstrate tritium self-sufficiency through on-site breeding, essential prerequisites for any future commercial fusion power plant [2].

The fundamental fusion reaction in DEMO relies on deuterium-tritium fusion generating high-energy fusion neutrons that carry approximately 80% of the reaction energy. These neutrons are harvested in the breeding blanket, a critical component that performs three essential functions simultaneously: energy extraction via coolant circulation, tritium breeding for fuel self-sustainment through lithium transmutation reactions, and neutron shielding to protect superconducting magnets from radiation damage [3,4]. As a result, the breeding blanket is among the most complex and technologically

* Corresponding author.
E-mail addresses: marino.corrado@polito.it (M. Corrado), pietro.arena@enea.it (P. Arena), aldo.collaku@polito.it (A. Collaku), alessandro.delnevo@enea.it (A. Del Nevo), ranieri.marinari@enea.it (R. Marinari), laura.savoldi@polito.it (L. Savoldi).

https://doi.org/10.1016/j.fusengdes.2026.115890
Received 29 December 2025; Received in revised form 1 June 2026; Accepted 16 June 2026
Available online 20 June 2026
0920-3796/© 2026 The Author(s). Published by Elsevier B.V. This is an open access article under the CC BY license (http://creativecommons.org/licenses/by/4.0/).

demanding components of DEMO. Currently, three breeding blanket concepts are under investigation within the EUROfusion consortium framework: the Water-Cooled Lead–Lithium (WCLL), the Helium-Cooled Pebble Bed (HCPB), and the recently developed Water-cooled Lead Ceramic Breeder (WLCB) [5,6]. Among these, the WCLL blanket concept has emerged as a promising candidate due to its reliance on proven pressurized water reactor (PWR) technology for coolant management, coupled with liquid lead–lithium (PbLi) alloy as both a tritium breeder and neutron multiplier [7]. The WCLL breeding blanket architecture is organized into distinct functional zones. The First Wall (FW) faces the plasma and must withstand intense heat fluxes up to several megawatts per square meter, protected by EUROFER as the primary structural material. Behind the FW lies the Breeding Zone (BZ), where PbLi circulates and tritium is produced through $^{6}Li(n,t)^{4}He$ and $^{7}Li(n,n')^{6}Li$ reactions. Water-cooled tubes remove heat from the BZ while thermally isolating the water coolant from the PbLi breeder. Water and PbLi manifolds distribute coolant and breeder fluid to parallel Breeding Units (BUs) arranged poloidally along the blanket segment [8,9]. A Back Supporting Structure (BSS) provides mechanical support and houses the attachment points to the vacuum vessel, as well as the fluid manifolds.

Recent advancements in WCLL blanket design, culminating in the 2024 conceptual design phase, have introduced substantial improvements over earlier configurations [5]. For the WCLL blanket, water serves as the primary coolant owing to its proven industrial applicability in PWR systems, superior heat transfer properties, and established engineering knowledge base [10]. The cooling system operates at a nominal inlet pressure of 15.5 MPa with inlet temperatures of 295 °C and an estimated outlet temperature of 328 °C [11].

A fundamental redesign replaced C-shaped double-walled tubes with helical Double-Wall Tubes (DWTs), reducing the total number from 22 to 24 per slice to 12, thereby significantly reducing the number of welds and improving structural reliability. This modification also reduces water inventory within the breeding zone, a critical factor for enhancing the Tritium Breeding Ratio (TBR) toward the design target of TBR$\geq$1.15, while simultaneously improving the cooling margin by maintaining component temperatures below the maximum recommended limit of 550 °C for EUROFER steel [12,13].

Designing manifolds for uniform mass flow distribution among multiple parallel cooling channels is a complex multidisciplinary challenge, as non-uniform flow can increase pressure losses, reduce thermal efficiency, and generate localized hot spots [14]. Manifold design optimization must balance competing objectives: achieving uniform mass flowrate distribution to avoid hot spots, minimizing total pressure drop to reduce pumping power requirements, maintaining structural integrity under thermal and electromagnetic loads, and accommodating toroidal and poloidal asymmetries imposed by the fusion neutron heat distribution [15].

A complementary innovation introduced in the 2024 conceptual design is the redesign of the breeding zone water manifold from a Z-type [5,16] to a U-type configuration. Thanks to a proper tailoring of the manifold cross section, the U-type manifold provides superior mass flow distribution uniformity among parallel breeding units compared to earlier designs, ensuring more balanced cooling capability across the blanket and reducing local hot spots that could compromise structural integrity. Fig. 1 shows schematically the cooling flow path in the U-manifold design of the WCLL-BB. The new manifold geometry places inlet and outlet sections at 2/3 of the total height to enhance pressure-driven flow distribution. The inlet flow is divided into two streams directed toward the upper and lower branches (see Fig. 1). Approximately two-thirds of the incoming water mass flow is directed toward the bottom portion of the segment (bottom branch), while the remaining one-third feeds the upper region (upper branch) [17].

The inlet flow within the upper branch is channeled through two separate conduits, while the inlet flow in the lower branch remains as a single channel (Fig. 1a). Both the upper branch and lower branch each feature two separate outlet channels that converge only at the blanket exit (Fig. 1b). The two outlet channels in the upper branch are positioned at the same elevation, whereas those in the lower branch are at different elevations.

Both in the upper and lower branches, the inlet channels communicate with the outlet channels through DWTs, as schematized in Fig. 1c and 1d.

Currently, a significant research gap exists in the experimental validation of the predictive CFD models used to design the novel U-type manifold of the WCLL blanket. Since manufacturing and testing a full-scale prototype is unfeasible due to its prohibitive physical dimensions and the capacity limits of available experimental platforms, the development of a geometrically scaled-down mock-up represents a mandatory step. This scaled prototype is essential to gather the empirical data required to validate the flow distribution predictions and ultimately consolidate the blanket design.

The principal objective of this work is to design a geometrically scaled TS representative of the WCLL breeding blanket U-type water manifold for the outboard segment, preserving the mass flow distribution of the Full Scale (FS) configuration. The scaled TS will be installed in the Water Loop facility under construction at ENEA Brasimone Research Center. In this study, we apply a 1:4 scaling factor to length, cross-sectional areas, and mass flowrate while preserving the velocity inlet and pressure drop behavior of the FS design. The scaling methodology is discussed, also based on previous studies [18], showing that preserving the pressure profile along manifolds is a fundamental principle for scaling down manifold geometries while maintaining representative mass flow rate distribution.

2. Methodology

2.1. Design and operation constraints

STEAM is a high-power branch of the Water Loop facility currently under construction within W-HYDRA platform at the ENEA Brasimone Research Center [18], designed to investigate the DEMO balance of plant water cooling system under both steady-state and transient conditions. The facility features a primary side operating with single-phase pressurized water at 15.5 MPa, thermally coupled with a secondary side working with two-phase water at 6.41 MPa. The nominal thermal power of the facility is 3.1 MW.

To experimentally validate its complex thermal-hydraulic behavior, the TS of the WCLL-BB will be installed in the STEAM facility. It will be integrated into the primary loop, specifically across the hot and cold legs, replacing the steam generator component (Fig. 2).Within this primary loop, the experimental conditions are controlled by two magnetically driven centrifugal pumps to regulate the mass flow rate, and two 1700 kW_e electrical heaters to ensure the target inlet temperature. The system pressure is maintained by a dedicated pressurizer connected to the hot leg, and the operating fluid is maintained in subcooled conditions.

Future study will include the construction of the TS and its experimental testing in the STEAM facility to validate the CFD predictions via differential pressure and mass flowrate measurements across the headers. The primary objective of the experimental campaign is to perform a sensitivity analysis on BUs mass flow rate on the total inlet mass flow rate (under constant pressure and inlet temperature). Due to the geometric complexity of the TS (78 equivalent pipes in 26 BUs), the definition of an optimal, non-redundant data acquisition layout is a challenging but vital task.

To monitor the thermal boundaries and ensure the isothermal assumption of the mock-up, six Type-K thermocouples (TCs) will be

[1] The terms first and second level refer to the radial position of the channels, with the first layer being radially inner and the second layer located further outward.

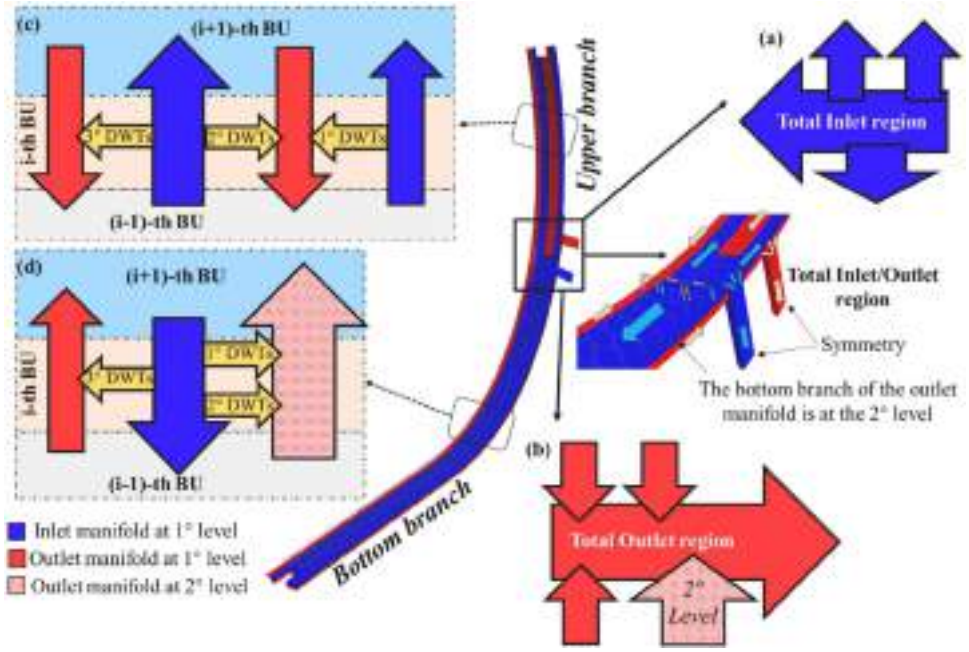


Fig. 1. Schematic representation of the flow path in the IM (a), in OM (b) and in a generic BU in the upper (c) and bottom (d) branches. To be noted that in the bottom branch, part of the OM is at a second (outer) level[1] with respect to the rest of the cooling circuit. (IM = Inner Manifold, OM = Outer Manifold, BU = Breading Unit).

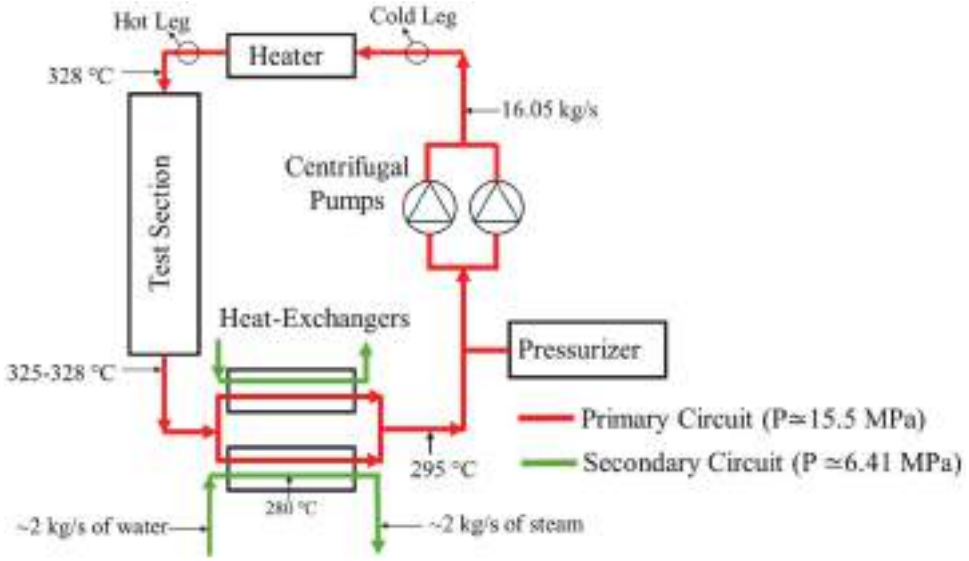


Fig. 2. Schematic of the STEAM thermal-hydraulic loops integrating the WCLL manifold Test Section.

installed along the manifolds. To map the macroscopic pressure trends, three differential pressure (DP) transducers will be employed: one measuring the global pressure drop across the entire mock-up, and the other two tracking the longitudinal pressure profiles along the IM and OM respectively. An indirect measurement methodology for the mass flowrate in the pipes mimicking the DWCs, based on localized pressure drops, will be adopted. To validate this indirect ΔP methodology and ensure experimental redundancy, a total of six EPPs will be fully instrumented with both a DP transducer and a mass flow meter. This allows for a continuous cross-check between the direct flow measurement and the ΔP-derived calculation. To achieve this without altering the complex piping geometry, non-intrusive clamp-on ultrasonic mass flow meters will be used. (This specific technology provides the operational flexibility to detach and relocate the sensors to different pipes during the experimental campaign, maximizing the data collection across various BUs without requiring structural modifications to the mock-up.)

Since the mock-up must be seamlessly integrated into the STEAM primary loop, its design and scaling parameters are strictly dictated by the operational boundaries and physical constraints of the host facility. Specifically, the design of the manifold TS must comply with the following limits:

- The maximum working pressure available is 18.5 MPa.
- The maximum working temperature available is 350 °C (for the maximum working pressure);
- The maximum available footprint for the TS is 2 m × 1.5 m;
- The maximum available height of the TS is 4 m;

- The maximum available mass flow is 20 kg/s;
- The maximum pressure drop is 0.15 MPa across the TS.
- The TS shall be coupled with the STEAM facility with a flanged connection of 6″ class 2500.
- The TS shall be an isothermal (zero-input power) component, heat losses through the component shall be reduced to an extent such as the maximum temperature loss along the manifold remains below 3 °C (about DWT kW);
- The maximum number of available signals to be acquired at the same time from the manifold TS is 50 (control constraint).

2.2. Equivalent porous pipe (EPP) approach for DWTs modeling

The coolant flow distribution between the Inner Manifold (IM) and Outer Manifold (OM) is managed by a total of 1248 Double-Wall Tubes (DWTs), whose function is to remove the heat generated within the Breeding Units (BUs). The DWTs are uniformly distributed among the 104 BUs, resulting in 12 tubes per BU. Within each BU, the tubes are arranged in six parallel pairs, each consisting of two twin channels, referred to as DWT-A and DWT-B, hydraulically connecting the IM and OM. Taking advantage of the geometrical symmetry of the BU (Fig. 3), only half of the domain was considered, resulting in three tube pairs being explicitly represented.

Since the distance between the inlet nozzles of DWT-A and DWT-B is very small (<2 cm) compared with the characteristic manifold dimensions, the fluid approaching the two tubes experiences essentially the same pressure conditions [19]. The same argument applies to the outlet nozzles. Therefore, each DWT pair operates under nearly identical pressure differences and can be represented by a single Equivalent Pipe (EP) reproducing the same hydraulic behaviour. The hydraulic characteristic of the EP is obtained by combining the hydraulic responses of DWT-A and DWT-B. Detailed CFD simulations of all DWT configurations were performed using STAR-CCM+ over a mass-flow-rate range between 45 and 150 g/s. Since the flow regime is turbulent throughout the investigated range, the k–ω SST turbulence model was adopted. For a given pressure drop, the mass flow rates through DWT-A and DWT-B were summed to obtain the hydraulic characteristic of the EP (Eq. (1)):

$$\dot{m}_{EP}(\Delta p) = \dot{m}_{DWT-A}(\Delta p) + \dot{m}_{DWT-B}(\Delta p) \tag{1}$$

The resulting EP characteristic, shown in Fig. 4a, covers a mass-flow-rate range extending from approximately 0.1 to 0.3 kg/s.

Although the EP accurately reproduces the hydraulic response of the DWT pair, explicitly resolving turbulent flow inside all the channels would still require a large computational effort. To reduce the computational burden while preserving the same hydraulic behaviour, the EP is further represented as an Equivalent Porous Pipe (EPP). The simplification procedure adopted in this work can be summarized as:

$$DWT - A + DWT - B \rightarrow Equivalent\ Pipe\ (EP) \rightarrow Equivalent\ Porous\ Pipe\ (EPP)$$

The EPP is modelled as a porous medium using the Darcy–Forchheimer formulation [20] (Eq. (2)):

$$\frac{\Delta p}{L} = P_i \bar{v}_{EPP}^2 + P_v \bar{v}_{EPP} \tag{2}$$

where (P_i) and (P_v) are the inertial and viscous resistance coefficients, respectively, and $\bar{v}_{EPP}$ is the average velocity inside the equivalent channel. This formulation introduces a momentum sink derived from volume-averaging of the microscopic flow field [21], accounting simultaneously for viscous friction (Darcy contribution) and inertial form drag (Forchheimer contribution). As a result, the total pressure drop can be reproduced solely from the average velocity in the conduit.

The Darcy–Forchheimer coefficients were obtained by fitting the EP hydraulic characteristic expressed in terms of pressure drop per unit length. More specifically, the pressure-drop curves of the EP were converted into (Δp/L) versus velocity relationships and fitted through an Ordinary Least Squares (OLS) procedure, yielding the coefficients reported in Table 1 and the regressions shown in Fig. 4b The resulting fits provide an excellent representation of the CFD data, with (R^2) values ranging between 0.95 and 0.98.

The three EPPs implemented in the present model correspond to the three different DWT pairs and therefore exhibit slightly different lengths and hydraulic resistances. Their geometrical and hydraulic characteristics are reported in Table 1.

The EPP is intended to reproduce the hydraulic resistance of the DWT pair and the resulting pressure-driven flow redistribution within the manifold, rather than the detailed local velocity and pressure fields inside the individual DWTs. This approximation is justified because the objective of the present work is the prediction of the global mass-flow-rate distribution among the breeding units. The use of equivalent porous channels for representing complex hydraulic networks is a well-established approach and has already been successfully applied to DEMO breeding blanket analyses [13,22].

Furthermore, no physical porosity is introduced in the model. The inlet area of the EPP is maintained equal to the sum of the inlet areas of DWT-A and DWT-B, thereby preserving the localized entrance and exit pressure losses associated with the manifold-to-tube connections. This allows the EPP representation to retain the same overall hydraulic response as the original DWT pair while significantly reducing the computational cost through a coarser mesh and a reduced number of governing equations.

2.3. Manifold and EPP pressure losses: key considerations for manifold scaling

The mass flow rate through each BU is primarily governed by the pressure difference between the IM and OM. Therefore, preserving the pressure profiles along the two manifolds is the key requirement for maintaining representative flow conditions in the scaled Test Section (TS).

A preliminary analytical assessment was carried out to identify the dominant contributions to the overall pressure drop. The total pressure loss within a BU consists of localized inlet and outlet losses at the EPP junctions and distributed losses along the EPPs. In the Full-Scale (FS) configuration, the total inlet mass flow rate is 68.1 kg/s, corresponding to an average flow rate of 0.654 kg/s per BU, approximately equally distributed among the three EPPs. Assuming a water density of 698 kg/m^3, the distributed pressure drop across a single EPP is estimated to be about 21 kPa using Eq. (2) and the coefficients reported in Table 1.

To estimate the localized pressure losses at the EPP–manifold junctions, the inlet and outlet loss coefficients ($K_{loc,in}$ and $K_{loc,out}$) were calculated using empirical correlations for dividing (Eq. (3) [23]) and combining (Eq. (4) [24]) flows, respectively. Here, $q = \dot{Q}_{EPP}/\dot{Q}_{man}$ denotes the ratio between the flow rate through a single EPP and that in the adjacent manifold section, whereas $a_{ratio} = 3A_{EPP}/A_{man}$ is the ratio between the total BU cross-sectional area and the manifold cross-sectional area. For the present geometry, $a_{ratio} = 2.6 \times 10^{-2}$.[2]:

$$K_{\mathrm{loc,in}} = \left[0.5 + 0.9\left(\frac{a_{\mathrm{ratio}}}{q}\right)^2\right](1-q^2) + 1.2\,q^2 \tag{3}$$

$$K_{\mathrm{loc,out}} = \max\left[1.0 - (1-q)^2\left(\frac{a_{\mathrm{ratio}}}{q}\right)^2,\ -2.5\right] \tag{4}$$

[2] $K_{loc,in}$ is an interpolation between two fluid-dynamic extremes. The first is the pure crossflow regime (q = 0), governed by Idelchik's empirical correlation for dividing tees. The second is the dead-end regime (q = 1), acting as a blind 90° turn with a constant resistance K_{dead} =1.2. A parabolic weighting on q is adopted because dynamic pressure losses intrinsically scale with kinetic energy (α v^2).

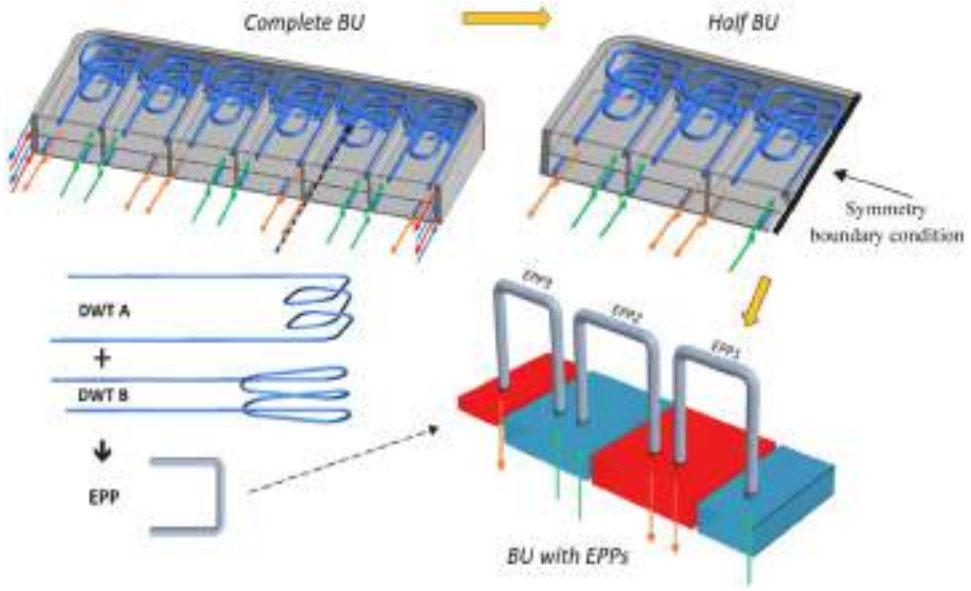


Fig. 3. Domain simplification: BU symmetry and lumped EPP for the DWTs pairs. (BU = Breading unit, EPP = Equivalent porous pipe, DWT = Double-walled tube).

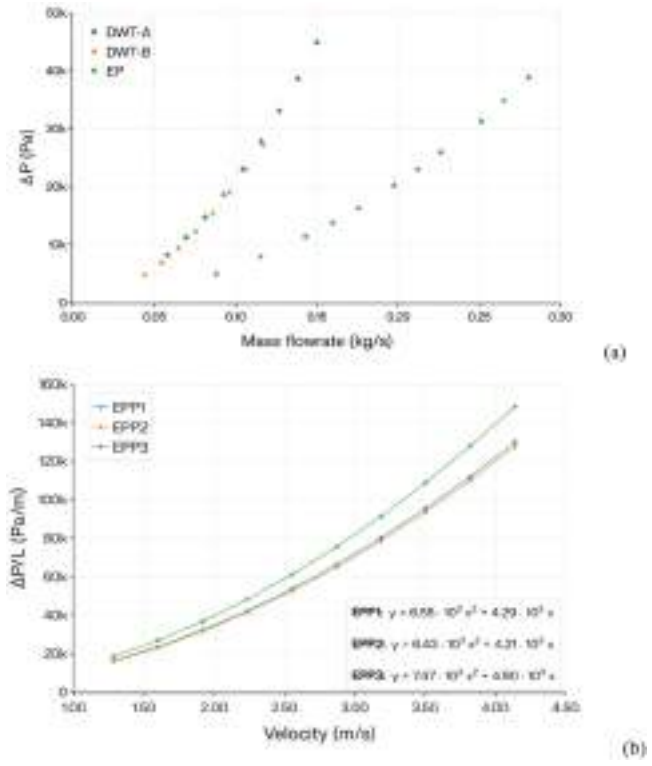


Fig. 4. Top (a): CFD-derived hydraulic characteristic curves (Δp vs. mass flowrate) for the DWT-A and DWT-B tubes, and the corresponding characteristic of an equivalent pipe. Bottom (b): hydraulic characteristic curves ($\Delta p/L$ vs. velocity) for EPP1, 2 and 3. Quadratic regression fits are provided for each dataset (R^2_{EP1}=0.97, R^2_{EP2} =0.95, R^2_{EP3}=0.98).

Table 1
Length, inertial and viscous resistances adopted in the hydraulic characterization of the Equivalent Porous Pipes (EPPs).

	Area [mm^2]	Length [mm]	$P_{inertial}$ [kg/m^4]	$P_{viscous}$ [kg/m^3/s]
EPP 1	98.57	309	6.55 10^3	4.30 10^3
EPP 2	98.57	315	6.43 10^3	4.21 10^3
EPP 3	98.57	271	7.47 10^3	4.90 10^3

As shown in Fig. 5, both loss coefficients vary with q along the 69 BUs of the lower branch. The inlet coefficient increases from $K_{loc,in} \approx 0.5$to 1.2, whereas the outlet coefficient varies from $K_{loc,out} \approx -2.1$ to 1.0. Since the maximum localized losses occur at the manifold extremity, subsequent estimates were based on BU #69 ($q = 1$), for which $K_{loc,in} =$ 1.2 and $K_{loc,out} = 1.0$.[3]:

The localized pressure losses at the inlet and outlet of each EPP, estimated through Eq. (5), are approximately 2.6 kPa and 2.2 kPa, respectively.

$$\Delta p_{loc} = K_{loc} \cdot \frac{1}{2} \rho v^2 \tag{5}$$

Therefore, the total pressure drop across a single BU is about 25.5 kPa, of which the dominant contribution arises from the distributed losses within the EPPs. This result confirms that preserving the hydraulic resistance of the DWTs through the EPP approach is essential to reproduce the BU pressure drop and, consequently, the flow distribution among the breeding units.

To quantify the relative importance of manifold losses, the distributed pressure drop along the lower branch was also estimated. Approximately two-thirds of the total inlet mass flow rate (45.4 kg/s) enters the lower branch, which has a rectangular cross-section of about 313 cm^2 and a hydraulic diameter $D_h$of 99 mm. The branch extends over two-thirds of the total blanket height L. Assuming a nearly uniform

[3] $K_{loc,out}$ represents the jet mixing effect. For large q(>2.5%), the incoming fluid acts as an obstacle, forcing the mainstream to turn sharply. This induces severe flow separation and violent turbulent mixing, which dissipate kinetic energy and cause a net pressure drop. For low q (<2.5%), the high-velocity fluid entering the manifold acts like an ejector pump, transferring momentum to the main flow and generating a localized pressure recovery, with an empirical lower limit set to −2.5.

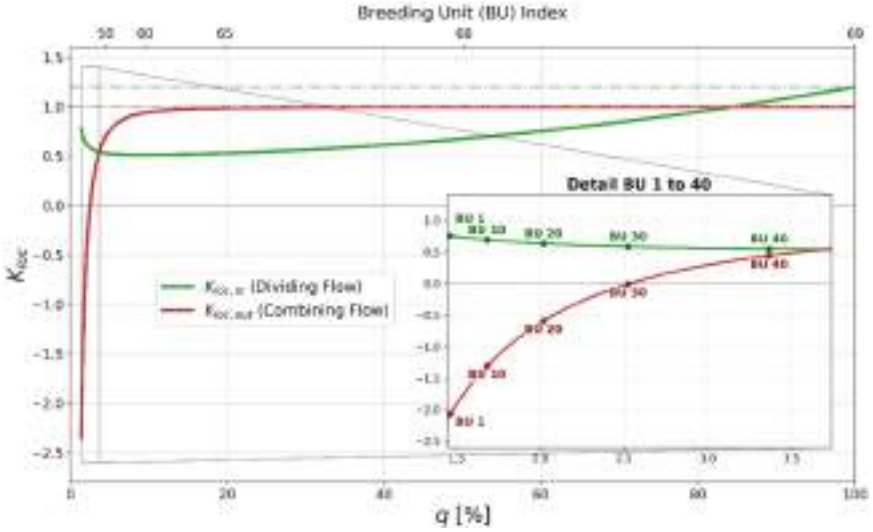


Fig. 5. Empirical estimation of $K_{loc,in}$ e $K_{loc,out}$ of the 69th BUs of the lower branch of the FS, as function of the q value. a_{ratio} is set to 2.6 10^{-2} by geometry. (FS= Full Size, BU = Breading Unit).

bleed-off from the IM to the OM, the average velocity decreases linearly from its inlet value $v_0 \approx 3$m/s to zero at the manifold extremity, see Eq. (6).

$$v(x) = \mathrm{v}_0\left(1 - \frac{x}{2/3L}\right) \tag{6}$$

Considering a water density of 698 kg/m^3 and a dynamic viscosity of 83.4 μPa·s, the Reynolds number at the manifold inlet is approximately 7.78 × 10^5 and decreases linearly with the local velocity toward the lower manifold extremity. Using the average Reynolds number (3.9 × 10^5), the Darcy friction factor for a smooth pipe is estimated from the Moody diagram [25] as λ = 0.013. The resulting distributed pressure drop along the lower branch is approximately 5.1 kPa (Eq. (7)).

$$\Delta p_{dist} = \frac{1}{2}\frac{\rho\lambda}{\mathrm{D_h}}\int_0^{\frac{2}{3}L} v(x)^2 dx = \frac{1}{2}\rho\lambda\frac{\mathrm{L}}{\mathrm{D_h}}\frac{2}{9}\mathrm{v_0}^2 \tag{7}$$

The comparison between the estimated manifold pressure drop (~5.1 kPa) and the pressure drop across a single BU (~25.5 kPa) clearly shows that the hydraulic behavior of the system is primarily governed by the losses within the BUs. Consequently, preserving the BU hydraulic resistance is the key requirement for maintaining the mass-flow-rate distribution in the scaled geometry.

For this reason, the same EPP geometries adopted in the Full-Scale configuration were retained in the Test Section. By preserving the average mass flow rate through each BU, the distributed pressure losses within the EPPs are also preserved. Although the scale-down modifies the ratio a_{ratio} from 2.6 × 10^{-2} (FS) to 1.0 × 10^{-1} (TS), resulting in average deviations of 8% and 19% in $K_{loc,in}$ and $K_{loc,out}$, respectively, these differences remain acceptable because localized manifold losses represent only a minor contribution to the overall pressure drop.

2.4. Navier-Stokes dimensionless equations and governing parameters

Core flow equations:

In the dimensionless form of the steady state Navier-Stokes equations (Eq. (8)), the flow in the manifolds is shown to be governed by the Reynolds (*Re*), Froude (*Fr*) and Euler (*Eu*) dimensionless numbers.

$$(\boldsymbol{v}^*\cdot\nabla^*)\boldsymbol{v}^* = -Eu\ \nabla^* p^*_{tot} + \frac{\nabla^{*2}\boldsymbol{v}^*}{Re} + \frac{D}{L}\frac{\boldsymbol{g}^*}{Fr^2} \tag{8}$$

The *Eu* number is defined as the ratio between pressure and inertia forces ($\Delta p/(\rho v^2)$), *Fr* is defined as the ratio between inertia and gravity forces $\left(v/\sqrt{gL}\right)$ and *Re* is defined as the ratio between inertia and viscous forces ($\rho v D/\mu$). D and *L* denote, respectively, the hydraulic diameter and the characteristic height of the system. The high value of *Re* (~10^5–10^6) implies that viscous forces are negligible compared to inertia forces, and does not significantly influence the pressure field, simplifying the Navier-Stokes equation to Euler equation (Eq. (9)).

$$(\boldsymbol{v}^*\cdot\nabla^*)\boldsymbol{v}^* \simeq -Eu\ \nabla^* p^*_{tot} + \frac{D}{L}\frac{\boldsymbol{g}^*}{Fr^2} \tag{9}$$

Since gravity force is conservative, it can be computed separately, as the static pressure $\left(p^*_{st}\right)$, decomposing Eq. (9) into Eqs. (10) and (11).

$$(\boldsymbol{v}^*\cdot\nabla^*)\boldsymbol{v}^* \simeq -Eu\ \nabla^*\left(p^*_{tot} - p^*_{st}\right) = -Eu\ \nabla^*\left(p^*_{din}\right) \tag{10}$$

$$Eu\ \nabla^* p^*_{st} \simeq +\frac{D}{L}\frac{\boldsymbol{g}^*}{Fr^2} \tag{11}$$

By preserving only *Eu*, the dimensionless dynamic pressure $\left(p^*_{din}\right)$ and velocity profiles are maintained during the scale down. As demonstrated in Section 2.3, pressure losses within the BUs largely dominate over distributed manifold losses. Therefore, the total hydraulic behavior of the system is primarily governed by the pressure drop across the BUs, allowing the Euler number to be preserved by maintaining the inlet velocity and the average mass flow rate through each BU (see Eq. (12)).

$$Eu = \frac{\Delta p_{tot}}{\rho v^2} \simeq \frac{\Delta p_{BU}(\dot{m}_{BU})}{\rho v^2} \tag{12}$$

Although the static pressure profile of the TS differs from that of the FS because *Fr* is not conserved in the scale-down, the inlet and outlet of each BU are located at the same elevation (see Fig. 1). This results in identical hydrostatic pressures at both ends of each BU. Therefore, Eq. (13) shows that the pressure difference driving the flow rate in the BUs is independent of elevation .

$$\begin{aligned}\Delta p_{BU} &= (p_{tot})_{IM} - (p_{tot})_{OM} = (p_{din} + p_{st})_{IM} - (p_{din} + p_{st})_{OM} \\ &= (p_{din})_{IM} - (p_{din})_{OM}\end{aligned} \tag{13}$$

Boundary layer equations:

Unlike the core flow, boundary-layer dynamics depend on Reynolds number and Froude number *Fr* similarity. The physical mechanism leading to flow separation and recirculation is schematically illustrated in Fig. 6, while the complete dimensional analysis reported in Appendix

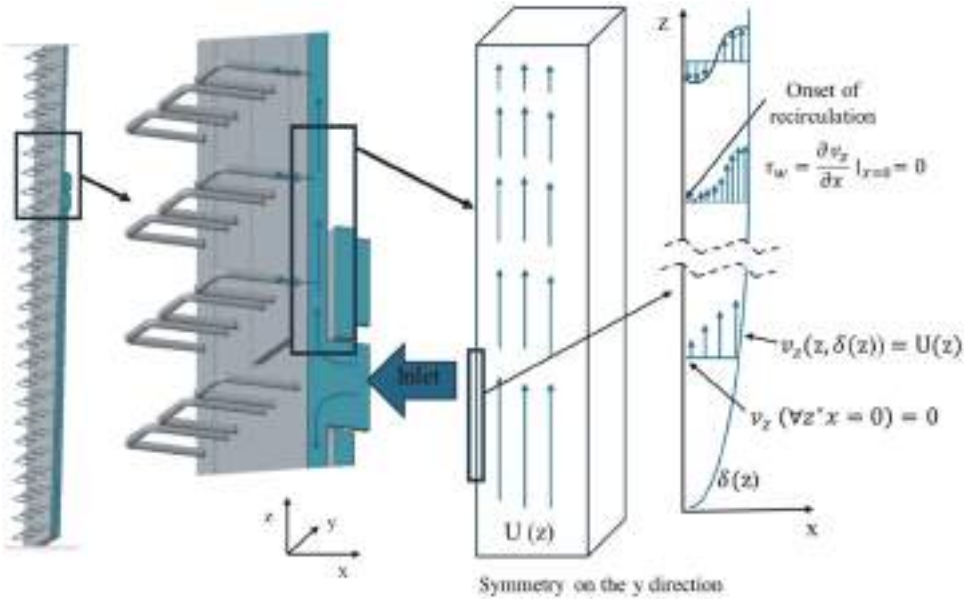


Fig. 6. Graphical representation of the boundary layer formation and onset of instability phenomena on the flow in the upper branch of the IM of TS (IM= Inner Manifold, TS= Test Section).

A shows that the onset of recirculation and instability phenomena depends on both *Re* and *Fr*.

In a constant bleed-off manifold, the progressive decrease in velocity generates an adverse pressure gradient that tends to destabilize the boundary layer. As a result, geometrically scaled configurations preserving *Eu* may still exhibit different instability onset locations and recirculation patterns.

In the present work, priority was given to preserving the core-flow similarity through *Eu*. The CFD results show that, although the recirculation structures differ between the FS and TS configurations, these effects do not significantly modify the pressure profile along the manifolds nor the resulting mass-flow-rate distribution among the breeding

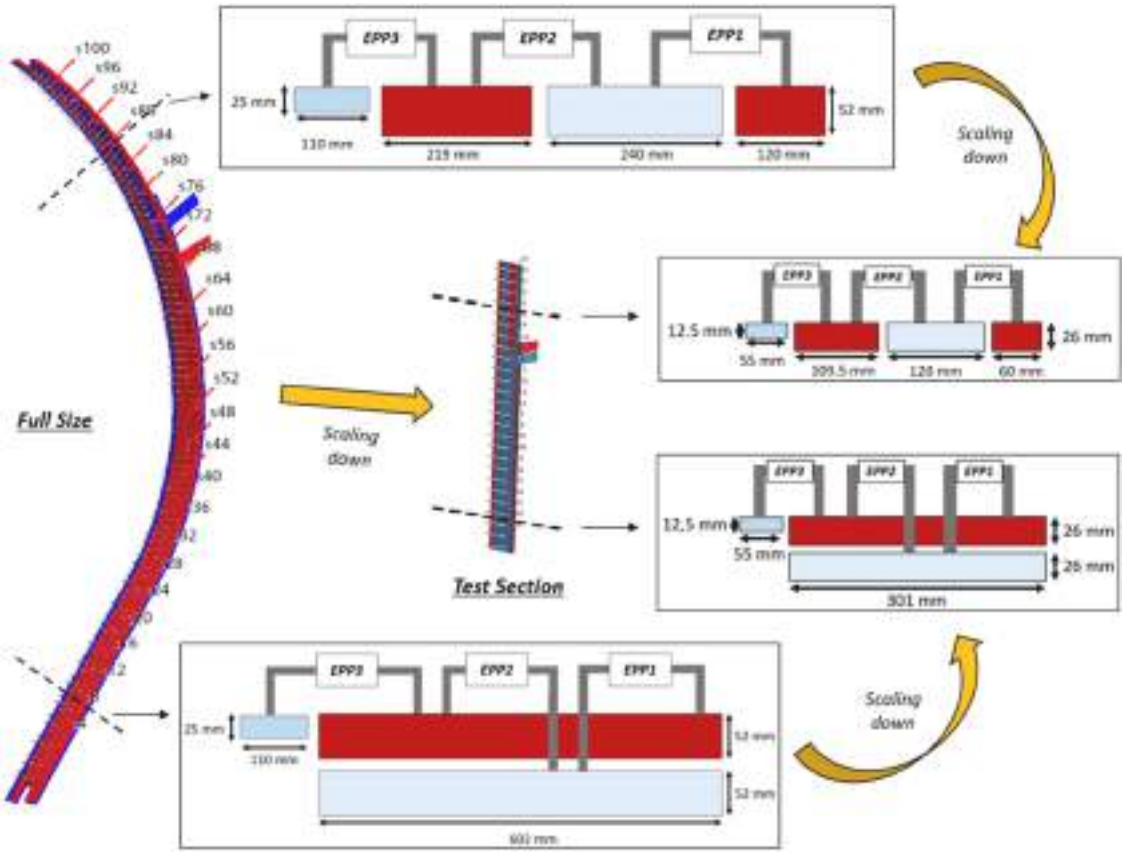


Fig. 7. Scaling down of the manifolds cross-sections.EPP diameter does not change in the scale down. Same hydraulic resistance must be ensured. (EPP = Equivalent Porous Pipe).

units.

2.5. Scaling down procedure and computational fluid dynamics (CFD) model

The blanket length was reduced by a scaling factor of ¼ (from ~14,040 mm to ~3510 mm) to accommodate the geometric constraints of the W-HYDRA platform (see Fig. 7). The WCLL-BB presents a curvature in the manifold, which is believed not to affect the mass flow rate distribution and thus omitted in the test-section design resulting in a linear configuration. To preserve the inlet velocity and velocity profile distributions required to replicate the dominant BU losses, the scaling approach did not reduce the individual BU geometry, but rather reduced the total number of BUs from 104 to 26.

Since each half-BU must receive the same mass flow rate, the total mass flow rate was reduced by a factor of 4, scaling from 68.1 kg/s to 17.025 kg/s.[4] To maintain the inlet velocity while reducing the mass flow rate, the manifold cross-sections are scaled by halving both the height and the width, thereby reducing the cross-sectional area by the same scaling factor of 4 while maintaining the proportions. This approach ensures that the cross-sectional area and the total mass flow rate are scaled by the same factor, thereby preserving the velocity profile distributions required to replicate the dominant localized losses. For both the TS and FS, the internal pipe roughness is assumed to be negligibly small. Table 2 summarized the main geometrical parameters (height, # of BUs and curvature) and inlet boundary condition (v, A, $\dot{m}$, Re) of the FS and TS. The scale down halves the inlet Re; however, because it remains sufficiently large as the flow regime remains turbulent in the manifolds, it does not influence the system dynamics, which remain dependent only on Eu (see Section 2.4).

The outlet pressure of the cooling water domain is set to 15.5 MPa for the TS configuration, as it was set for the FS case in [5]. Water thermophysical properties at 15.5 MPa and 311 °C (mean value between inlet 295 °C and estimated outlet temperature 328 °C) were utilized. The commercial software STAR-CCM+ is used for the CFD simulations. The turbulent flow regime in the clear channels is resolved using the κ-ω SST turbulence closure, as already done in [26]. The flow in the EPP is described using of the Darcy-Forchheimer relation.

Since detailed 3D thermal-hydraulic analyses [25] have confirmed that coolant wall temperatures remain safely below the saturation threshold, definitively ruling out the occurrence of localized boiling within the WCLL Breeding Zone, steady and monophase (liquid water only) conditions have been simulated. Note that in the HYDRA test facility the fluid will not be heated in the TS, but rather before entering it, guaranteeing the absence of two-phase phenomena in the TS. In the real DEMO configuration, the IM and OM operate at 295 °C and 328 °C, respectively, inducing moderate changes in density (~12%) and viscosity (~20%) and affecting the hydraulic response of the system. Under uniform BU heating, the mass flow-rate distribution is estimated not to change, whereas under poloidally non-uniform heating the hotter BUs exhibit lower hydraulic resistance and thus a higher mass flow rate. Since the DEMO neutron wall loading on the outer blanket varies poloidally from about 1.35 MW/m² to 0.76 MW/m² [27], future thermo-fluid dynamic simulations will also be required to assess the deviation on flow distribution induced by heat anisotropy.

For both the FS and TS models, the core manifold domain was discretized using a global base size of 6 mm (see Fig. 8). To accurately capture the inlet effects, the mesh was progressively refined down to 1 mm at the entrance of the EPPs, using a volume reduction rate of 1.2. The boundary layer was modeled using the "All y^+ Wall Treatment", supported by a near-wall mesh consisting of 8 orthogonal prism layers with a stretching factor of 1.5 applied to all wetted surfaces. Post-processing checks confirmed that the wall y^+ values remained within the range of 0.2 to 65 throughout the entire system. This meshing strategy is consistent with the grid sensitivity study conducted in [28] and resulted in a total grid size of 72.7 million cells for the FS model and 4.6 million cells for the TS model.

Table 2
Main characteristics of the FS and TS geometries. (FS= Full Size, TS= Test Section, BU =Breading Unit). The mass flow rates for FS and TS refer to the real values (although only half of the geometry was modeled due to symmetry).

Propriety	Units	FS	TS
Height	mm	14,040	3510
Curvature	-	YES	NO
N° of BUs	-	104	26
Inlet velocity	m/s	5.134	5.134
Inlet mass flowrate	kg/s	136.2	34.05
Inlet area	mm^2	38,013	9503
Inlet hydraulic diameter	mm	220	110
Inlet Reynolds number Re	-	$9.45\ 10^6$	$4.73\ 10^6$
Euler number Eu	-	5.60	4.95

3. Results and discussion

This section presents the CFD results obtained for the scaled TS and their comparison with the FS configuration. In particular, the fluid dynamics in the TS configuration have been simulated and compared with data obtained in [5] for the FS design.

Both the total mass flow rate per breeding unit and the mass flow rate through each EPP were extracted at the outlet surfaces and compared with the corresponding FS results, to verify that the scaling-down process successfully preserves the flow distribution. Pressure and velocity profiles along the IM and OM were extracted as surface averages on cross-sections located between breeding units, as shown in Fig. 9.

In the FS design, 63.5% of the mass flow rate is directed into the lower branch, while the remaining 36.5% flows into the upper branch. The TS shows a very similar flow split: 64.5% in the lower branch and 35.5% in the upper branch. These results confirm the expected flow split between the upper and lower branches and indicate that the hydraulic resistance of each branch is primarily governed by the relative number of breeding units.

The computed mass flow rate distribution of the ranks of EPPs −1, −2, and −3 is shown in Fig. 10a. Both in FS and TS, EPPs −1 and −2 exhibit similar flowrates, whereas EPP3 experiences reduced flow because its smaller OM channel increases the hydraulic resistance of the path. An overall very good agreement between the FS and TS results is observed. The relative error, defined in Eq. (14), remains below 10% for >90% of the EPPs, indicating that the local mass flow rate distribution is effectively preserved by the scaling-down approach. In Eq. (18), $\dot{m}_{t.s.}$ refers to the EPPs mass flow rate of the TS, while $\overline{\dot{m}_{f.s.}}$ is the average of the four consecutive EPPs of the FS. Larger deviations are confined to the inlet region and to the downstream end of the bottom branch, where jet entrance effects and local flow instabilities become more pronounced (Fig. 10b).

$$\epsilon = \frac{\dot{m}_{t.s.} - \overline{\dot{m}_{f.s.}}}{\overline{\dot{m}_{f.s.}}} \tag{14}$$

Marginally larger relative errors for the EPP3 (up to 18%) are found

[4] These values represent the mass flow rates applied in the computational model, which takes advantage of geometrical symmetry (simulating only a fraction of the domain). For the real, full-scale mass flow rates of the system, please refer to Table 2.

[5] The EPP mass flow rates vary from 113 to 287 g/s, except at the inlet section, and fall within the validated hydraulic characteristics shown in Fig. 4a.

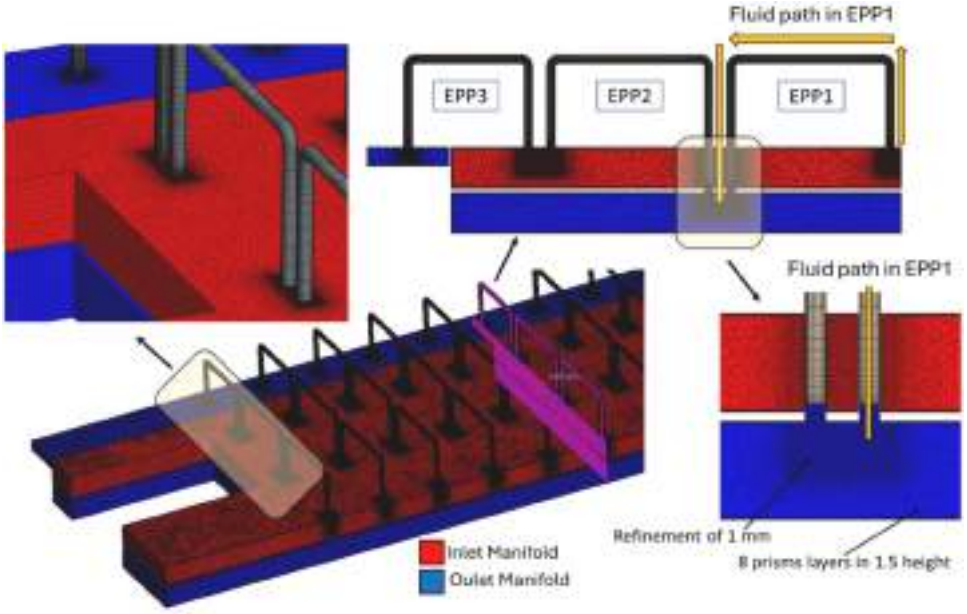


Fig. 8. Polyhedral mesh details for the TS, showing the inlet (red) and outlet (blue) manifolds. Cross-sections highlight the local refinement strategy: 1 mm cell size at the EPPs entrances and 8 orthogonal prism layers to resolve the wall boundary layer. (TS = Test Section, EPP = Equivalent Porous Pipe).

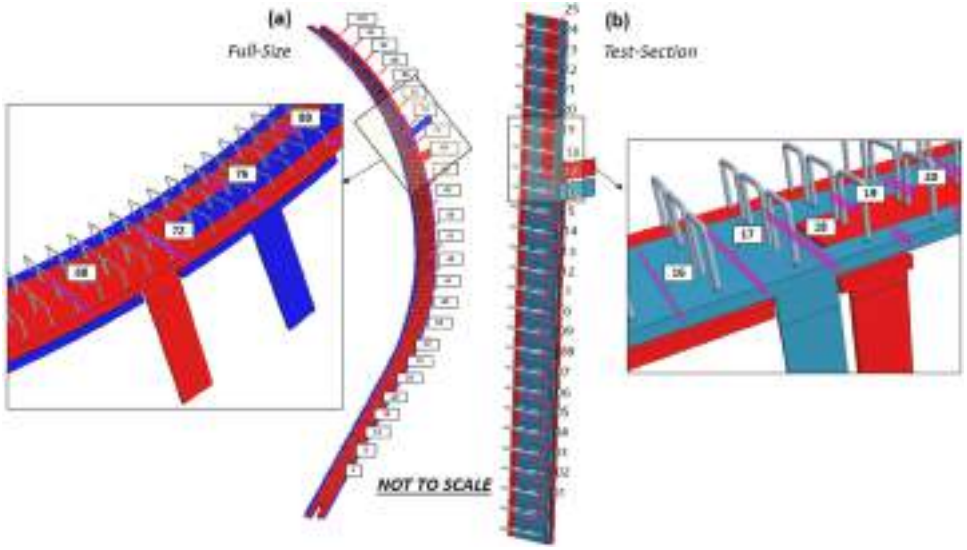


Fig. 9. Total number of 25 cross-sections used to extract surface average quantities along the IM and OM every 4 BUs in the FS (a) (4, 8, 12, 16…100) and every BU in the TS (b) (1, 2, 3, 4…25). Figure not to scale. (IM = Inner Manifold, OM = Outer Manifold, BU = Breading Unit, FS= Full Size, TS= Test Section).

in correspondence to the downstream end of the bottom branch and for the EPP1 in the inlet region (Fig. 10b). Furthermore, the inlet jet effect involves two BUs in the FS and one BU (representing 4 BUs of the FS) in the TS designs, meaning that the scaling down amplifies the jet entrance effect.

Note also that the rank of EPP3 in the test-section exhibits higher mass flow rates with respect to the FS, conversely, the mass flow rates in rank of EPP2 results to be lower. This local unbalance smears out when looking at the total mass flow rate in each BU (meaning the sum of EPP −1, −2 and −3). Fig. 11a reports the comparison between the BUs mass flow rate in the two geometries while Fig. 11b reports its relative error computed in the same way as for the single EPPs mass flow rates. The results show relative errors below 3% for all BUs but BU #18, already targeted as non representative of the FS design.

The total pressure drop of the TS has been calculated to be equal to 0.91 bar, ~12% less than the FS one, equal to 1.03 bar. This deviation is consistent with previous geometric scale-downs of WCLL Z-type manifolds configuration [26]. Fig. 12a reports the relative pressure (p_{abs}-p_{outlet}) profile in the IM and OM. The pressure profiles remain nearly constant along both inlet and outlet manifolds in the two configurations, indicating that the manifolds behave as quasi-infinite reservoirs. Concerning the comparison between the two geometries, a good agreement

[6] Data shows distributed losses are negligible compared with the losses across the BU. More specifically, the estimated 5.1 kPa distributed pressure drop in the OM of TS agrees with the simulations, while the IM of TS exhibits a flat profile.

[7] The comparison between the empirical estimate and the CFD prediction of the total pressure loss in BU #69 in the FS, although yielding the same order of magnitude, reveals an underestimation of 33%, making empirical estimates unreliable for precise pressure drop estimation in this geometry.

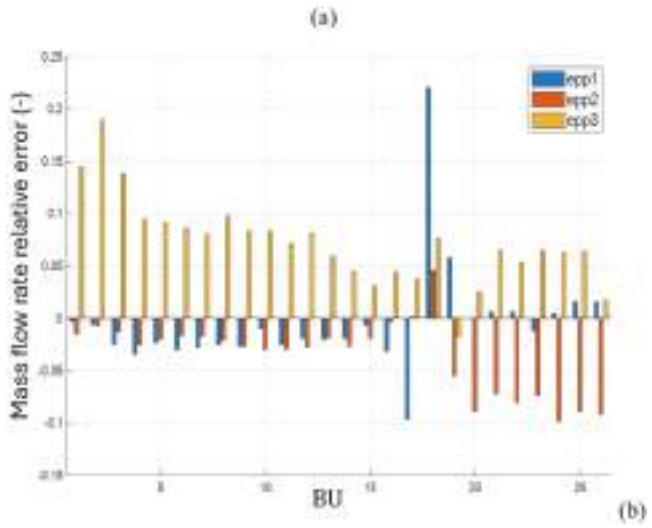


Fig. 10. On the top (a): Mass flow rate distribution[5] of ranks of EPP −1 (red), −2 (black) and −3 (blue) along the BB computed for the FS (squares) and TS (dots) designs. On the bottom (b): TS EPPs mass flow rate error with respect to the FS design. (EPP =Equivalent Porous Pipe, FS = Full Size, TS = Test Section).

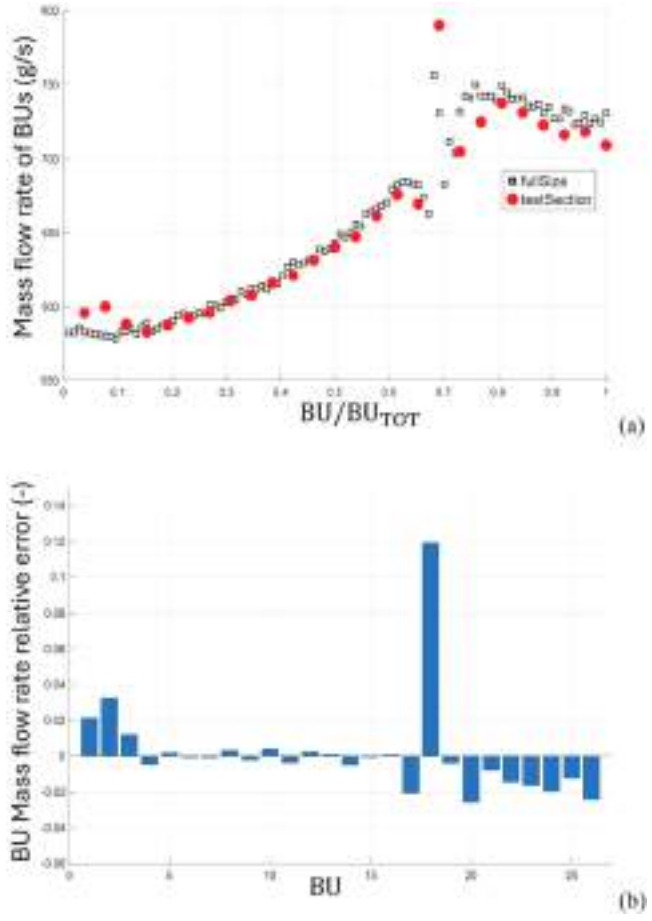


Fig. 11. On the top(a): Mass flow rate distribution in the BUs (EPP1 + EPP2 + EPP3) along the BB computed for the FS (squares) and TS (dots) designs. On the bottom(b): Test-section BUs total mass flow rate error with respect to the FS design. (BU= Breading Unit, EPP =Equivalent Porous Pipe, FS = Full Size, TS= Test Section).

is found in the OM, especially in the bottom branch where the same

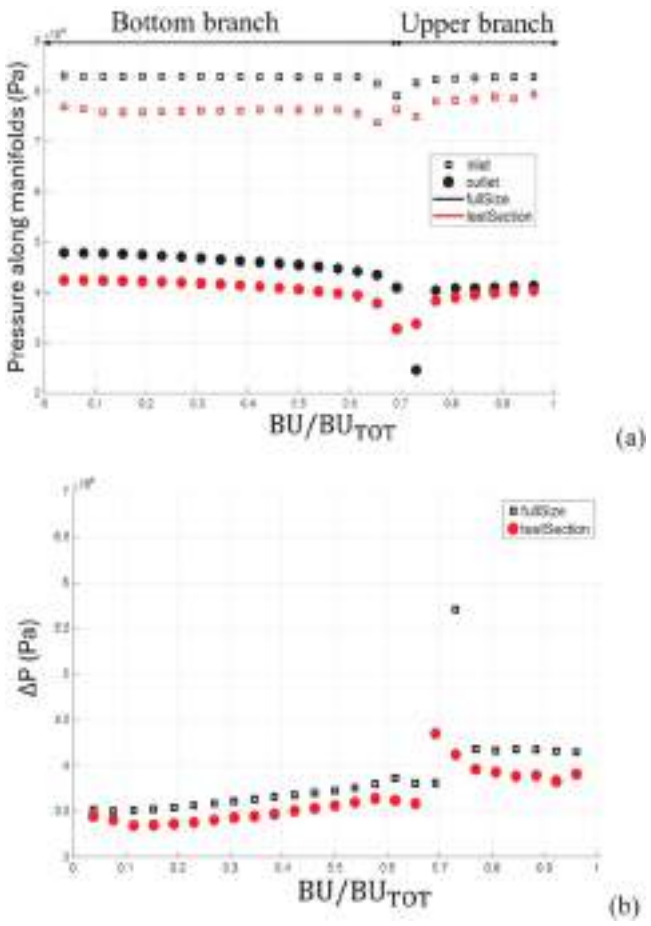


Fig. 12. Relative pressure profiles (a) in the IM (squares) and OM (dots) in the FS[6] (black) and TS (red). Pressure difference between the two manifolds (b) in the FS[7] (squares) and TS designs. (IM = Inlet Manifold, OM = Outer Manifold, FS = Full Size, TS = Test Section).

pressure is found, while lower values are found in the IM of the test-section.

There is a pressure difference of ~6000 Pa along the OM between the TS and the FS (see Fig. 12a), caused by an excessive pressure loss at the inlet of the IM of the latter case. The same pressure difference (~6000 Pa) is present also on the IM. This discrepancy highlights an intrinsic trade-off of velocity-based scaling: while the manifold velocity profile is preserved, full similarity in dimensionless parameters (e.g. Reynolds number) is not. As anticipated by the pressure-loss analysis of Section 2.3, preserving the pressure difference between IM and OM is sufficient to preserve the mass-flow-rate distribution among the BUs (Fig. 10).

Fig. 13 reports the velocity profiles computed in the IM and OM. It is shown that the velocity decreases nearly linearly from the inlet toward the downstream end of the upper and lower branches of the FS design, thereby reinforcing the nearly-uniform bleed-off assumption adopted in Section Methodology. It can be noted that the test-section exhibits a larger spike (6.2 m/s) in correspondence of the entering region of the IM, located at 2/3 of the total height, compared to the FS geometry (3.4 m/s). In all the OM and the upper branch of the IM, the velocity profile is perfectly identical between the FS and TS across its entire length. Conversely, in the bottom branch of IM the velocity profiles coincide down to 40% of the total height, then the test-section presents higher velocities (Fig. 13).

Fluid streamlines in that region (Fig. 14a) highlight the presence of a large vortex in the first 16 BUs of the IM of the FS design. The same phenomenon, still present in the TS geometry, is constrained in the first

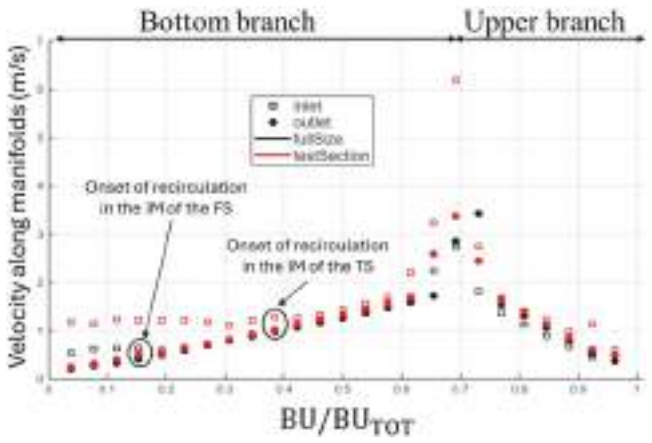


Fig. 13. Velocity profile computed along the inlet (squares) and the outlet (dots) manifolds for the FS (black) and the TS (red) design. (FS = Full Size, TS = Test Section).

extremities. Since the scaling halved the TS inlet *Re*, the TS hits this threshold earlier. This expands the backflow region in the TS (BU/BU$_{tot}$ < 0.4 and > 0.9) compared to the FS (BU/BU$_{tot}$ < 0.2), see Fig. 14.

Although recirculation modifies the velocity field at the IM edges, its impact on the pressure field is marginal; the pressure distribution remains nearly flat in both the TS and FS, so the BU mass flow-rate distribution is essentially preserved.

4. Conclusions and perspective

A geometrical scaling-down strategy for a U-type water manifold of the EU DEMO WCLL breeding blanket was developed to design a reduced-size Test Section (TS) suitable for experimental investigations within the constraints of available testing facilities.

As demonstrated in Section 2.3, pressure losses within the breeding units dominate over distributed manifold losses and therefore govern the coolant mass-flow-rate distribution. Based on this finding, a 1:4 scaling factor was applied to the manifold length, cross-sectional areas, total mass flow rate, and number of breeding units, while preserving the

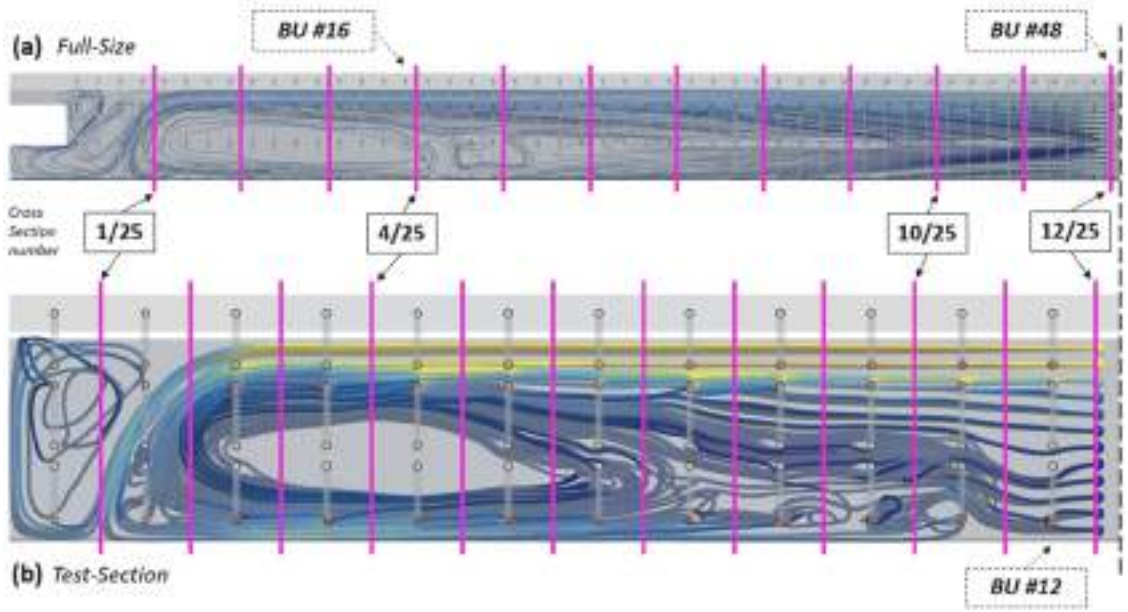


Fig. 14. Streamlines displayed in the bottom branch IM (up to ~50% of the total height) in the FS (a) and TS (b) design. In pink the cross-section locations. (FS = Full Size, TS = Test Section).

6 BUs (being representative of first 24 BUs of the FS). Here, vortices and some backflow recirculation are found up to BU #11 (Fig. 14b). This recirculation effect, which increases during the scale down,[8] is the dominant cause for the higher velocity profile at the bottom branch end of the IM (see Fig. 15).

In the IM, the flow rate is progressively tapped off, resulting in a reduction of the average sectional velocity and, consequently, the characteristic Reynolds number (estimated with the average sectional velocity and the hydraulic diameter), while the flow cross-sectional area remains constant. Fig. 15 shows that in both the TS and FS configuration, backflow phenomena are observed to occur in the bottom branch around $Re \sim 5 \times 10^5$. Vortex generation noticeably increases the mean liquid velocity, maintaining a relatively high *Re* even at the channel pressure difference between the Inlet and Outlet Manifolds that drives the flow distribution among the BUs.

Steady-state single-phase CFD simulations confirmed the effectiveness of the proposed methodology. The total mass flow rate per breeding unit is preserved within 3% relative error for all units except the inlet one, which is affected by enhanced jet entrance effects. At the local level, the mass flow rate distribution through 96% of the Equivalent Porous Pipes (EPPs) is reproduced within 10% relative error, demonstrating that the main hydraulic characteristics of the Full-Scale (FS) manifold are accurately retained in the scaled geometry.

The results show that preserving the manifold pressure profiles is sufficient to reproduce the pressure-driven flow distribution among parallel breeding units. Although local deviations in the velocity field arise near the inlet region and manifold extremities due to intensified jet effects and vortex-induced recirculation, these phenomena do not significantly affect the pressure field nor compromise the overall hydraulic representativeness of the TS.

Future work will focus on the construction and operation of the Test Section in the W-HYDRA facility, enabling the experimental validation

[8] The TS has four time the Fr^2 and half the *Re* of the FS. These conditions do not preserve similarity in the boundary-layer equations (Eq. A8), leading to an earlier onset of instability in the TS case and, consequently, to an earlier occurrence of recirculation phenomena in the core flow.

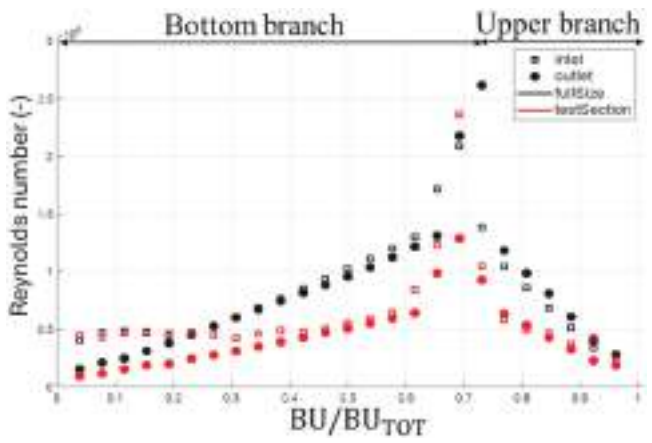


Fig. 15. Reynolds profile computed along the inlet (squares) and the outlet (dots) manifolds for the FS (black) and the TS (red) design. The section-averaged velocity of the channels (inlet and outlet) is used as the reference for Reynolds estimation. (FS = Full Size, TS = Test Section).

of the proposed scaling methodology and CFD modelling framework through direct comparison between numerical predictions and measured flow-distribution data.

CRediT authorship contribution statement

Marino Corrado: Conceptualization, Investigation, Methodology, Software, Validation, Visualization, Writing – original draft. **Pietro Arena:** Conceptualization, Resources. **Aldo Collaku:** Conceptualization, Data curation, Investigation, Methodology, Writing – original draft. **Alessandro Del Nevo:** Funding acquisition, Supervision. **Ranieri Marinari:** Methodology, Writing – review & editing. **Laura Savoldi:** Formal analysis, Funding acquisition, Methodology, Project administration, Supervision, Writing – review & editing.

Declaration of competing interest

The authors declare that they have no known competing financial interests or personal relationships that could have appeared to influence the work reported in this paper.

Acknowledgments

This work was carried in the framework of the EUROfusion Consortium, funded by the European Union via the Euratom Research and Training Programme under Grant 101052200 — EUROfusion. The use of ChatGPT to improve and check the English language is acknowledged.

Appendix A. Boundary-layer similarity analysis

The dimensional analysis presented in Section 2.4 demonstrates that preserving the Euler number is sufficient to maintain the similarity of the core flow, whereas the development of the boundary layer and the onset of instability phenomena depend on additional dimensionless parameters. The derivation of the governing dimensionless equations is reported in this appendix.

The flow within the boundary layer is governed by the local balance between inertia, pressure-gradient and viscous forces. Under the classical boundary-layer assumptions, the two-dimensional momentum and continuity equations can be written as:

$$v_z\frac{\partial v_z}{\partial z}+v_x\frac{\partial v_z}{\partial x}=-\frac{1}{\rho}\frac{\partial p_{tot}}{\partial z}+\frac{\mu}{\rho}\frac{\partial^2 v_z}{\partial x^2} \tag{A1}$$

$$\frac{\partial v_z}{\partial z}+\frac{\partial v_x}{\partial x}=0 \tag{A2}$$

where (z) is the streamwise coordinate along the manifold and (x) is the wall-normal coordinate. The following dimensionless variables are introduced:

$$v_z{}^*=\frac{v_z}{U_0},\ v_x{}^*=\frac{v_x}{V_0},\ z^*=\frac{z}{L},\ x^*=\frac{x}{\delta} \tag{A3}$$

where:

- (U_0) is the characteristic streamwise velocity,
- (V_0) is the characteristic wall-normal velocity,
- (L) is the characteristic manifold height,
- (δ) is the boundary-layer thickness.

Substituting Eq. (A3) into Eq. (A1) and using Eq. (A2) to eliminate (V_0), the dimensionless momentum equation becomes:

$$v_z{}^*\frac{\partial v_z{}^*}{\partial z^*}+v_x{}^*\frac{\partial v_z{}^*}{\partial x^*}=-\frac{D}{\rho {U_0}^2}\frac{\partial p_{tot}}{\partial z}+\frac{1}{Re}\frac{DL}{\delta^2}\frac{\partial^2 v_z{}^*}{\partial x^{*2}} \tag{A4}$$

Where Re is the Reynolds number based on the manifold hydraulic diameter (D).

To obtain a thin but dynamically consistent boundary layer, the viscous term must remain of the same order of magnitude as the inertial terms, leading to:

$$\delta\sim\sqrt{\frac{DL}{Re}} \tag{A5}$$

The pressure gradient appearing in Eq. (A4) is determined by the macroscopic core flow. Neglecting viscous effects in the core region, the streamwise momentum equation reduces to:

$$U\frac{\partial U}{\partial z} = -\frac{1}{\rho}\frac{\partial p_{tot}}{\partial z} + g \tag{A6}$$

using the identity:

$$U\frac{\partial U}{\partial z} = \frac{1}{2}\frac{\partial U^2}{\partial z} \tag{A7}$$

Substituting Eq. (A7) into Eq. (A4) and introducing the Froude number *Fr* yields:

$$v_z{}^*\frac{\partial v_z{}^*}{\partial z^*} + v_x{}^*\frac{\partial v_z{}^*}{\partial x^*} = \frac{1}{2}\frac{\partial U^{*2}}{\partial z^*} - \frac{1}{Fr^2} + \frac{1}{Re}\frac{DL}{\delta^2}\frac{\partial^2 v_z{}^*}{\partial x^{*2}} \tag{A8}$$

Eq. (A8) shows that the evolution of the boundary layer depends on the combined action of:

- the adverse pressure gradient generated by the progressive bleed-off of flow along the manifold;
- gravitational effects represented by the Froude number;
- viscous diffusion represented by the Reynolds number.

The velocity profile is obtained by solving Eq. (A8) subject to the no-slip condition at the wall:

$$v_z{}^*(\forall z^*, x^* = 0) = 0 \tag{A9}$$

and the matching condition at the edge of the boundary layer:

$$v_z{}^*(z^*, 1) = U^*(z^*) \tag{A10}$$

Boundary-layer separation and the onset of recirculation occur when the wall shear stress vanishes:

$$\tau_w = \frac{\partial v_z}{\partial x}|_{x=0} = 0 \tag{A11}$$

Or, in dimensionless form:

$$\tau_w = \frac{\partial v_z{}^*}{\partial x^*}|_{x^*=0} = 0 \tag{A12}$$

Eq. (A8) shows that the onset of instability depends on the interplay between Reynolds and Froude effects through the boundary-layer thickness and the gravitational contribution.

Data availability

Data will be made available on request.

References

[1] A.J.H. Donné, The European roadmap towards fusion electricity, Philos. Trans. R. Soc. Math. Phys. Eng. Sci. 377 (2141) (2019) 20170432, https://doi.org/10.1098/rsta.2017.0432.

[2] G. Federici, et al., Overview of the design approach and prioritization of R&D activities towards an EU DEMO, Fusion Eng. Des. 109-111 (2016) 1464–1474, https://doi.org/10.1016/j.fusengdes.2015.11.050.

[3] G. Federici, L. Boccaccini, F. Cismondi, M. Gasparotto, Y. Poitevin, I. Ricapito, An overview of the EU breeding blanket design strategy as an integral part of the DEMO design effort, Fusion Eng. Des. 141 (2019) 30–42, https://doi.org/10.1016/j.fusengdes.2019.01.141.

[4] L. Giancarli, et al., Breeding blanket modules testing in ITER: an international program on the way to DEMO, Fusion Eng. Des. 81 (1) (2006) 393–405, https://doi.org/10.1016/j.fusengdes.2005.08.096.

[5] P. Arena, et al., Design of the WCLL BB in view of the conceptual design phase, Fusion Eng. Des. 218 (2025) 115205, https://doi.org/10.1016/j.fusengdes.2025.115205.

[6] G. Zhou, Y. Lu, F.A. Hernández, A water cooled lead ceramic breeder blanket for European DEMO, Fusion Eng. Des. 168 (2021) 112397, https://doi.org/10.1016/j.fusengdes.2021.112397.

[7] P. Arena, et al., The DEMO water-cooled lead–Lithium breeding blanket: design status at the end of the pre-conceptual design phase, Appl. Sci. 11 (24) (2021) 11592, https://doi.org/10.3390/app112411592.

[8] A. Del Nevo, et al., Recent progress in developing a feasible and integrated conceptual design of the WCLL BB in EUROfusion project, Fusion Eng. Des. 146 (2019) 1805–1809, https://doi.org/10.1016/j.fusengdes.2019.03.040.

[9] P. Arena, et al., Design and integration of the EU-DEMO water-cooled lead lithium breeding blanket, Energies 16 (4) (2023) 2069, https://doi.org/10.3390/en16042069.

[10] E. Martelli, et al., Study of EU DEMO WCLL breeding blanket and primary heat transfer system integration, Fusion Eng. Des. 136 (2018) 828–833, https://doi.org/10.1016/j.fusengdes.2018.04.016.

[11] E. Vallone, G. Bongiovì, P.A. Di Maio, I. Moscato, A. Quartararo, S. Vacca, Development of a thermal-hydraulic model of the EU-DEMO water cooled lithium lead breeding blanket primary heat transport system, Fusion Eng. Des. 193 (2023) 113686, https://doi.org/10.1016/j.fusengdes.2023.113686.

[12] R. Forte, P. Arena, A. Del Nevo, P.A. Di Maio, On the effects of the Double-Walled tubes lay-out on the DEMO WCLL breeding blanket module thermal behavior, Fusion Eng. Des. 146 (2019) 883–886, https://doi.org/10.1016/j.fusengdes.2019.01.105.

[13] P.A. Di Maio, P. Arena, G. Bongiovì, P. Chiovaro, A. Del Nevo, R. Forte, Optimization of the breeder zone cooling tubes of the DEMO water-cooled Lithium lead breeding blanket, Fusion Eng. Des. 109-111 (2016) 227–231, https://doi.org/10.1016/j.fusengdes.2016.03.021.

[14] A. Froio, F. Casella, F. Cismondi, A. Del Nevo, L. Savoldi, R. Zanino, Dynamic thermal-hydraulic modelling of the EU DEMO WCLL breeding blanket cooling loops, Fusion Eng. Des. 124 (2017) 887–891, https://doi.org/10.1016/j.fusengdes.2017.01.062.

[15] F. Edemetti, P. Micheli, A. Del Nevo, G. Caruso, Optimization of the first wall cooling system for the DEMO WCLL blanket, Fusion Eng. Des. 161 (2020) 111903, https://doi.org/10.1016/j.fusengdes.2020.111903.

[16] A. Del Nevo, et al., Recent progress in developing a feasible and integrated conceptual design of the WCLL BB in EUROfusion project, Fusion Eng. Des. 146 (2019) 1805–1809, https://doi.org/10.1016/j.fusengdes.2019.03.040.

[17] A. Allio, P. Arena, A. Del Nevo, L. Savoldi, Hybrid modelling for the manifolds and coolant flow distribution in the Water-cooled Lead-Lithium of the EU-DEMO reactor, in: Proceedings of the 19th International Topical Meeting on Nuclear Reactor Thermal Hydraulics (NURETH-19), Brussels, Belgium Paper 19001, 2022.

[18] Arena, W-HYDRA: a new experimental platform for the water-cooled lead lithium breeding blanket, Nucl. Fusion 076043 (2024).

[19] R.A. Bajura, A model for flow distribution in manifolds, J. Eng. Power 93 (1) (1971) 7–12, https://doi.org/10.1115/1.3445410.

[20] H. Huang, J. Ayoub, Applicability of the Forchheimer equation for non-darcy flow in porous media, SPE J. 13 (01) (2008) 112–122, https://doi.org/10.2118/102715-PA.

[21] S. Whitaker, The Forchheimer equation: a theoretical development, Transp. Porous. Media 25 (1996) 27–61.

[22] A. Sharma, A. S K Saha, A. Sharma, D. Sharma, P. Chaudhuri, Thermal-hydraulic characteristics of purge gas in a rectangular packed pebble bed of a fusion reactor using DEM-CFD and porous medium analyses, Fusion Eng. Des. 160 (2020) 111848, https://doi.org/10.1016/j.fusengdes.2020.111848.

[23] B.R. Munson, T.H. Okiishi, W.W. Huebsch, A.P. Rothmayer, Fundamentals of Fluid Mechanics, 7th ed, John Wiley & Sons, 2013.

[24] D.S. Miller, Internal Flow Systems, 2nd ed., Gulf Publishing Company, Houston, TX, USA, 1990. *ISBN: 978-0872010208*.
[25] F. Edemetti, I. Di Piazza, A. Del Nevo, G. Caruso, Thermal-hydraulic analysis of the DEMO WCLL elementary cell: BZ tubes layout optimization, Fusion Eng. Des. 160 (2020) 111956, https://doi.org/10.1016/j.fusengdes.2020.111956.
[26] A. Collaku, P. Arena, A. Del Nevo, R. Marinari, L. Savoldi, Design of a test section for the experimental investigation of the WCLL Manifold hydraulic features, Energies 16 (5) (2023) 2246, https://doi.org/10.3390/en16052246.
[27] U. Fisher, Neutronic performance issues of the breeding blanket options for the european DEMO Fusion Power Plant, in: 12th International Symposium on Fusion Nuclear Technology (ISFNT 12), 2012.
[28] F. Edemetti, Thermal-hydraulic study and optimization of the DEMO water cooled lithium-lead breeding blanket, UNI Tesi Sapienza (2021).